DOI: XX.XXXX
Article type: Communication

Sub-nanosecond Tuning of Microwave Resonators Fabricated on Ruddlesden-Popper Dielectric Thin Films

Aaron M. Hagerstrom, Xifeng. Lu, Natalie. M. Dawley, Hari Nair, Jordi Mateu, Robert Horansky, Charles. A. E. Little, James. C. Booth, Christian J. Long, Darrell G. Schlom, and Nathan. D. Orloff*

Dr. A. M. Hagerstrom, Dr. X. Lu, Prof. J. Mateu, Dr. R. Horansky, Dr. C. A. E. Little, Dr. J. C. Booth, Dr. C. J. Long, Dr. N. D. Orloff
Communications Technology Laboratory, National Institute of Standards and Technology, Boulder, Colorado 80305, USA
E-mail: Aaron.Hagerstrom@nist.gov
Dr. X. Lu
Department of Physics, University of Colorado, Boulder, Colorado 80305, USA
N. M. Dawley, Dr. H. Nair, Prof. D. G. Schlom
Department of Materials Science Engineering, Cornell University, Ithaca, New York 14853, USA
Prof. J. Mateu
Signal Theory and Communication Department, Universitat Politecnica de Catalunya, Castelldefels, Barcelona, Spain
Dr. C. A. E. Little
Department of Mechanical Engineering, University of Colorado, Boulder, Colorado 80305, USA

Keywords: ruddlesden-popper, tunable dielectric, microwave, telecommunications, tuning speed

Voltage-tunable dielectric materials are widely used for microwave-frequency signal processing. Among tunable dielectric thin films, $(SrTiO_3)_nSrO$ Ruddlesden-Popper (RP) superlattices have exceptionally low loss at high frequencies. This paper reports the first realization of resonators, a ubiquitous building block of microwave components, fabricated on RP films, and an analysis of their static and dynamic tuning behavior. The resonators have approximately 2.5 % tuning of the resonance frequency at room temperature and 20 % tuning at 200 K, and a tuning time scale of less than a nanosecond, which is limited for the current measurements by the circuit rather than material properties.

Consumer demand for faster data rates and lower latencies is pushing the telecommunications industry to develop technologies that work at higher operating frequencies[1] with improved spectral efficiency. Tunable components are important for addressing these challenges. For example, tunable phase shifters are used in beamforming and multiple-input-multiple-output coding schemes in next-generation mobile handsets[2–5]. Ferroelectric materials have been widely studied as a way to build voltage-tunable devices.[6] Unfortunately, many of the most widely-used tunable dielectrics have high loss at frequencies above 10 GHz,[7–10] which limits their usefulness in this frequency range. Notable exceptions are $(SrTiO_3)_nSrO$ Ruddlesden-Popper (RP) superlattices, which have an exceptionally low dielectric loss (loss tangent ~ 0.05 at 125 GHz[10]) at room temperature compared to other tunable dielectrics. In addition to the advantage of enabling low-loss devices, this low loss at mm-wave frequencies suggests another potential advantage of RP films. The lack of a relaxation frequency in the GHz range suggests that the material's dielectric constant can change on sub-nanosecond timescales. Fast tuning speeds could allow for faster optimization of a wireless channel in a changing environment. In the following, we demonstrate resonant structures, a ubiquitous building block for filters, duplexers, multiplexers and other components in front-end electronics,[12,13] fabricated on a RP film. Measurements of these components show tuning of approximately 20 % at 200 K and 2.5 % at room temperature for DC tuning voltages of 15 V, and that the tuning timescale of these devices is limited to less than a nanosecond by circuit configuration rather than by the material properties.

Unlike the most common tunable dielectric material, $Ba_xSr_{1-x}TiO_3$, the $(SrTiO_3)_nSrO$ system remains a viable tunable dielectric with low dielectric loss at frequencies well into the GHz range.[6,10] In contrast to $Ba_xSr_{1-x}TiO_3$, $(SrTiO_3)_nSrO$ is composed of $SrTiO_3$ layers broken up periodically by $(SrO)_2$ crystallographic shear planes. It is believed that these shear planes accommodate local nonstoichiometry that would otherwise be incorporated as point defects, allowing the active $SrTiO_3$ material between the $(SrO)_2$ layers to remain pristine and

thus able to retain low loss into to the gigahertz regime. The $(SrO)_2$ layers act as a low loss, low dielectric constant spacer. In bulk, $(SrTiO_3)_nSrO$ is non-polar and not tunable. Shown theoretically[11] and proven experimentally,[10] it was found that the application of biaxial tensile strain gives rise to in-plane ferroelectricity, and that the Curie temperature increases with strain and with the index n of the $(SrTiO_3)_nSrO$ phases. The RPs act as relaxor ferroelectrics due to the $(SrO)_2$ layers breaking up the TiO_2 chains, allowing each $SrTiO_3$ block to act as a nanodomain.[10,11] For tunable dielectrics it is optimal for the Curie temperature to be below, but close to, room temperature to prevent loss due to ferroelectric domain wall motion, while retaining high polarizability. Here, we grow $n = 6$ $(SrTiO_3)_nSrO$ on ScO_2-terminated (110) $DyScO_3$ substrates[12,13] (with lattice constant 3.949 Å) to provide ~1.1 % tensile strain to shift the ferroelectric Curie temperature to approximately 200 K (**Figure 1**c). The film was grown 50 nm thick on (110) $DyScO_3$ using an oxide molecular-beam epitaxy system at a substrate temperature of 875 °C in an oxidant (~ 90% O_2 + 10% O_3) background pressure of 1×10^{-4} Pa (1×10^{-6} Torr). The film was found to have high structural perfection by x-ray diffraction (**Figure 1**a) and rocking curve scans (**Figure 1**b). Precise atomic layering was achieved through source shuttering and calibration of individual SrO and TiO_2 monolayers shutter times using reflection high-energy electron diffraction (RHEED) intensity oscillations.[14] Growth was initiated by supplying two SrO monolayers to account for the SrO floating layer that remains throughout the deposition.[15,16]

Our resonator consists of a capacitively-coupled coplanar-waveguide transmission line that supports resonant standing wave modes (**Figure 1**d). In general, transmission lines can be modeled using four parameters: a distributed resistance R, inductance L, conductance G, and capacitance C per unit length. A travelling wave with angular frequency ω will vary with the position x along the line as $e^{\gamma x}$, where γ is the propagation constant given by $\gamma = \alpha + j\beta = \sqrt{(R + j\omega L)(G + j\omega C)}$, and α and β are the attenuation and phase constants, respectively. In

the limit that the losses and coupling capacitance are small, the lowest order resonant mode of the device is determined by $\beta\ell = \pi$. At resonance, the voltage is maximum at the ends of the device ($x = 0$ and $x = \ell$), and the current is a maximum at the center. To apply a bias voltage, we added a bias arm in the middle of the resonator (**Figure. 1**d). In the paraelectric state of the RP film (above approximately 200 K), a non-zero bias voltage V_{DC} between the center conductor and the outer conductor of the transmission line decreases the permittivity of the RP film. A decreasing permittivity decreases the distributed capacitance and shifts the resonance frequency upward, because a higher frequency is needed to satisfy the resonance condition.

In keeping with the requirements of mobile technology, several features of our design allow the resonator to be physically compact (1 mm in length). First, we minimized the gap width (the distance between the center conductor and the ground plane) to 2.7 μm to increase the distributed capacitance, and therefore β. We also employed an interdigitated design with 10 μm- wide fingers that penetrate 60 μm into the ground plane, further increasing C (**Figure 1**d). The lowest resonance frequency was between 12 GHz and 15 GHz, depending on the temperature and DC bias. To increase the operating frequency, one can decrease the length of the resonator, increase the gap width, or decrease the length of the interdigitated fingers. We fabricated our tunable resonators (**Figure 1**d) on a 10 mm × 10 mm, 50 nm thick n = 6 RP film on a (110) $DyScO_3$ substrate by optical lithography. We used a contact aligner to pattern the photoresist, and deposited the conductors, consisting of a (5 ± 1) nm titanium adhesion layer followed by a (400 ± 10) nm gold layer, by electron-beam evaporation using a liftoff process to define the structures.

We characterized the linear behavior of our resonator in terms of scattering (S) parameters. The S parameters are defined so that $b_n = \sum_m S_{nm}\, a_m$, where b_n is the signal leaving the n^{th} port of the device, and a_m is the signal entering the m^{th} port of the device.[17] The quantities $|a|^2$ and $|b|^2$ have dimensions of power, and can be interpreted as the power

emitted by a source and the power absorbed by a receiver, respectively. For a 2-port resonator, the parameter (S_{21}) describes the frequency-dependent power transmission and phase shift of the resonator.

Measurements of S_{21} (Figure 2a) show a peak in the transmission near the resonance frequency. We measured the transmission as a function of temperature and DC bias voltage V_{DC} in a cryogenic probe station with a vector network analyzer (VNA) and used an on-wafer multiline Thru-Reflect-Line calibration[18] to error-correct the S parameters. The on-wafer calibration standards were fabricated on a $LaAlO_3$ reference substrate. Because this RP film has a Curie temperature of about 200 K, we measured the S parameters at room temperature (paraelectric state), 200 K, and 150 K (ferroelectric state). At each temperature, V_{DC} was increased from -15 V to 15 V. For each bias state, we extracted the resonance frequency (Figure 2b). We observed that the resonance frequency increased with increasing $|V_{DC}|$, and found that this tunability increased near the Curie temperature.

The resonator's static tuning behavior (**Figure 2**a) can be described by a compact circuit model (see Supporting Information), where the resonator's tuning behavior was described by the voltage-dependent capacitance per unit length of the waveguide. We extracted C from a fit to the model (the black line in **Figure 2**a). At a bias voltage of 15 V, C decreased by approximately 25 %, 30 %, and 4 % for 150 K, 200 K, and 293 K, respectively; the corresponding increases in the resonance frequencies were approximately 15 %, 20 %, and 2.5 %. In addition to the resonance frequencies, we also quantified the loss in the resonator. Resonator losses are typically quantified by the unloaded quality factor, Q_u[17], which is the theoretical limiting value of the quality factor as the coupling strength goes to 0. Using the circuit model, we calculate that Q_u of these resonators falls in the range of approximately 6 to 10, depending on the temperature and bias voltage. The dielectric loss is low ($\tan\delta < 0.05$) at room temperature[11], so we attribute most of the loss to conduction loss in the metallic conductors. In this work, we have chosen to focus primarily on the frequency tuning rather

than the Q_u tuning because the device geometry is dominated by metal losses, making it difficult to accurately quantify the losses due to the RP film. The conductor losses could in principle be decreased by using thicker conductors, or by using a larger gap in the transmission line structure, although the latter would sacrifice tuning. Thicker RP films would enable the same amount of tuning with a larger gap and therefore a higher Q_u.

One of the attractive features of voltage-tunable dielectrics is their fast tuning, which is much harder to quantify than the static tunability. One approach is to apply a step-like excitation to a capacitor loaded with the material and measure the time-domain response. Ultrafast optoelectronic methods can measure dynamics on the scale of 10's of ps.[19] Even with fast pulsed lasers and oscilloscopes, interpretation of these experiments is challenging, and both physical- and circuit-level modelling is necessary to separate the contributions of the circuit parameters, material behavior, and the finite rise time of the excitation signal.[20] We argue that small-signal sinusoidal excitation offers a path toward tuning speed characterization which is more general and less dependent on modelling.

Under some very general assumptions, the response of a nonlinear system to two-tone excitation fully determines its behavior under arbitrary excitation in the small signal limit.[21] In the time domain, filters are typically described by a linear, time-invariant transfer function. Such a description is not adequate if the filter's characteristics are modified by a time-varying tuning signal. Equation (1) is a simple generalization of linear theory that relates the incident signal $a_1(t)$, the tuning signal $a_3(t)$, and the output signal $b_2(t)$. The function $K_1(t)$ describes the linear transfer function of the filter and $K_2(t', t'')$ describes how the transfer function is modified by the tuning signal.

$$b_2(t) = \int_{-\infty}^{t} dt' K_1(t-t') a_1(t') + \int_{-\infty}^{t} dt' \int_{-\infty}^{t} dt'' K_2(t-t', t-t'') a_3(t') a_1(t'') \quad \#(1)$$

In Equation (1), $b(t)$ and $a(t)$ have the same physical meaning as they do for S parameters, but are expressed in the time domain rather than the frequency domain. We

performed measurements with sinusoidal input signals, so a frequency-domain description is more appropriate.

$$b_2(\omega) = S_{21}(\omega)\, a_1(\omega) + \int_{-\infty}^{\infty} d\omega' \int_{-\infty}^{\infty} d\omega'' \delta(\omega - \omega' - \omega'') \widehat{K}_2(\omega', \omega'') a_3(\omega') a_1(\omega'') \quad \#(2)$$

Equation (2) is mathematically equivalent to Equation (1), but provides a description in terms of quantities that are easier to access experimentally. The linear transfer function of the filter is described by the Fourier transform of $K_1(t)$ in Equation (1), which is also is the scattering parameter $S_{21}(\omega)$. The tuning of the filter is characterized by $\widehat{K}_2(\omega', \omega'')$, and the magnitude of this quantity can be inferred from frequency-domain measurements.

The frequency dependence of $\widehat{K}_2$ describes the transient tuning behavior in a device. Qualitatively, the function $|\widehat{K}_2(\omega_{sig}, \omega_{tune})|^2$, with ω_{sig} held constant, shows a peak where $\omega_{sig} \pm \omega_{tune}$ is at the resonance frequency and the bandwidth of this peak in $\widehat{K}_2$ indicates the rate at which tuning transient behavior decays, with a narrower peak corresponding to a longer transient time. Thus, the bandwidth of $\widehat{K}_2$ can be used to define a tuning time. To measure $\widehat{K}_2$ (**Figure 1**e), we excite the resonator with a continuous wave signal at a frequency f_{sig} = 13.25 GHz (near resonance), with a power of $P_1 = 8$ dBm. We also excited the tuning port with a continuous wave signal at a frequency f_{tune}, which we sweep over a range of frequencies from 6 to 18 GHz. The RF tuning signal had a power of $P_3 = 0$ dBm at the source, and was combined with a DC tuning voltage with a bias tee. Using a spectrum analyzer, we measure the sideband signals at $f_{sig} \pm f_{tune}$. According to Equation (2), the power of the signal measured at the spectrum analyzer, P_2, is given by $P_2 = |\widehat{K}_2(\omega_{sig}, \omega_{tune})|^2 P_3 P_1$. In terms of required equipment, our measurement technique is simple, but still achieves high dynamic range (> 70 dB) and a broad bandwidth (18 GHz).

To quantify tuning time, we define $\tau_{10\,dB} = 1/\Delta_{10\,dB}$, where $\Delta_{10\,dB}$ is the full width of the peak in P_2 at 10 dB below the maximum. While this quantity does not directly

characterize the time-domain response, it provides information on relevant dynamical timescales, and can be compared over a range of temperatures and voltages. Circuit simulations show that $\tau_{10\,dB}$ is comparable to the time it takes for transients to decay by 50%, although there is no simple relationship between these two quantities across the range of relevant parameters.

Figure 3a shows the frequency dependences of the sidebands, and **Figure 3**c shows the dependence of the tuning time on bias voltage and temperature. The circuit takes longer to tune at higher bias voltages and is most sensitive to bias voltage at 200 K. In order to understand this dependence, we developed a circuit model that accounts for both the non-linearity of the RP film and the spatial structure of the signals involved (see Supporting Information). In this model, the small-signal tunability is parameterized by $C'(V_{DC})$, the derivative of the distributed capacitance with respect to voltage with a DC bias of V_{DC}. Within the resonator, the voltage and current waves are modelled by a voltage-dependent capacitance per unit length, $C(V) = C(V_{DC}) + C'(V_{DC})V$.

Figure 3a shows a comparison between the nonlinear circuit model and the data. There are no fitting parameters to describe the shape of the curve. All of the parameters, except C'/C , are determined by the fit to the S parameters shown in **Figure 2**a. The model reproduces the shape of the data, including the faster-than-Lorenzian decay of the sideband amplitudes, and the widening due to the offset between the resonance frequency and the signal frequency. The tuning times seen in this model are consistent with those seen in experiment (**Figure 3**c).

From the circuit model, we expect the sideband voltage to be proportional to C'/C, because the phase of the signal at f_{sig} is modulated by the tuning signal through the variable capacitance per unit length of the device. Since the amplitude of the tuning signal, V_{tune}, is small, the change in propagation constant will be proportional to C'. Indeed, we found that the

overall sideband power increased rapidly with V_{DC} when V_{DC} was < 2.5 V, consistent with the parabolic dependence of C on V_{DC} for low V_{DC} (**Figure 2**c). The sideband power also peaks at higher V_{DC}, around 5 V, which is again consistent with the trends seen in the DC tuning (**Figure 2**c). In contrast to the higher temperatures, at 150 K a relatively strong tuning response is seen at V_{DC} = 0 V. Second order nonlinear effects require a breaking of inversion symmetry. The nonlinear response at V_{DC} = 0 V is consistent with remanent polarization in the ferroelectric state, which acts as a source of built-in bias field.

In conclusion, we have shown that compact resonators with a resonance frequency around 12 GHz fabricated on RP films can be tuned over 20 % at 200 K, and 2.5 % at room temperature by applying a voltage bias. We also introduced a non-linear measurement scheme to evaluate the tuning speed and formulated a compact model of the device that is consistent with these measurements. The tuning speed measurement demonstrated that the characteristic timescale of the device tuning was less than one nanosecond, showing the feasibility of creating high-tuning-speed phase shifters and filters with RP films. In the model, the device tuning speed is purely due to the linear characteristics of the waveguide and coupling capacitors, while the material's dielectric constant is assumed to change instantaneously in response to an applied bias. This suggests that the intrinsic tuning time of the RP film is well below the sub-nanosecond tuning time of the device, offering promise for even faster devices. Future work will be focused on reducing the device losses and quantifying the intrinsic tuning speed of the RP films.

Supporting Information
Supporting Information is available from the Wiley Online Library or from the author.

Acknowledgements
We acknowledge discussions pertaining to device fabrication with T. M. Wallis at the National Institute of Standards and Technology (NIST). All microwave measurements were conducted at the Communications Technology Laboratory at NIST, Boulder. Microelectronics

fabrication was performed Boulder Microfabrication Facility. This publication was supported by an agreement with Cornell University, MATERIALS SCIENCE & ENGINEERING, under Prime Agreement N00014-14-1-0674 from OFFICE OF NAVAL RESEARCH DOD. This work was also supported by the NIST Materials Genome Initiative. The work at Cornell was supported by Office of Naval Research award N00014-14-1-0674. This work made use of the Cornell Center for Materials Research (CCMR) Shared Facilities, which are supported through the NSF MRSEC program (DMR-1719875). Substrate preparation was performed in part at the Cornell NanoScale Facility, a member of the National Nanotechnology Coordinated Infrastructure (NNCI), which is supported by the NSF (Grant ECCS-15420819).

Received: ((will be filled in by the editorial staff))
Revised: ((will be filled in by the editorial staff))
Published online: ((will be filled in by the editorial staff))

References

[1] T. S. Rappaport, S. Sun, R. Mayzus, H. Zhao, Y. Azar, K. Wang, G. N. Wong, J. K. Schulz, M. Samimi, F. Gutierrez, *IEEE Access* **2013**, *1*, 335.

[2] W. Roh, J. Y. Seol, J. Park, B. Lee, J. Lee, Y. Kim, J. Cho, K. Cheun, F. Aryanfar, *IEEE Communications Magazine* **2014**, *52*, 106.

[3] A. Babakhani, X. Guan, A. Komijani, A. Natarajan, A. Hajimiri, *IEEE Journal of Solid-State Circuits* **2006**, *41*, 2795.

[4] M. Sazegar, Y. Zheng, C. Kohler, H. Maune, M. Nikfalazar, J. R. Binder, R. Jakoby, *IEEE Transactions on Antennas and Propagation* **2012**, *60*, 5690.

[5] D. Gesbert, M. Shafi, D. Shiu, P. J. Smith, A. Naguib, *IEEE Journal on Selected Areas in Communications* **2003**, *21*, 281.

[6] A. K. Tagantsev, V. O. Sherman, K. F. Astafiev, J. Venkatesh, N. Setter, *Journal of Electroceramics* **2003**, *11*, 5.

[7] J. C. Booth, I. Takeuchi, K.-S. Chang, *Appl. Phys. Lett.* **2005**, *87*, 082908.

[8] S. S. Gevorgian, E. L. Kollberg, *IEEE Transactions on Microwave Theory and Techniques* **2001**, *49*, 2117.

[9] C. V. Weiss, M. B. Okatan, S. P. Alpay, M. W. Cole, E. Ngo, R. C. Toonen, *J Mater Sci* **2009**, *44*, 5364.

[10] C.-H. Lee, N. D. Orloff, T. Birol, Y. Zhu, V. Goian, E. Rocas, R. Haislmaier, E. Vlahos, J. A. Mundy, L. F. Kourkoutis, Y. Nie, M. D. Biegalski, J. Zhang, M. Bernhagen, N. A. Benedek, Y. Kim, J. D. Brock, R. Uecker, X. X. Xi, V. Gopalan, D. Nuzhnyy, S. Kamba, D. A. Muller, I. Takeuchi, J. C. Booth, C. J. Fennie, D. G. Schlom, *Nature* **2013**, *502*, 532.

[11] T. Birol, N. A. Benedek, C. J. Fennie, *Phys. Rev. Lett.* **2011**, *107*, 257602.

[12] J. E. Kleibeuker, G. Koster, W. Siemons, D. Dubbink, B. Kuiper, J. L. Blok, C.-H. Yang, J. Ravichandran, R. Ramesh, J. E. ten Elshof, D. H. A. Blank, G. Rijnders, *Adv. Funct. Mater.* **2010**, *20*, 3490.

[13] J. E. Kleibeuker, B. Kuiper, S. Harkema, D. H. A. Blank, G. Koster, G. Rijnders, P. Tinnemans, E. Vlieg, P. B. Rossen, W. Siemons, G. Portale, J. Ravichandran, J. M. Szepieniec, R. Ramesh, *Phys. Rev. B* **2012**, *85*, 165413.

[14] J. H. Haeni, C. D. Theis, D. G. Schlom, *Journal of Electroceramics* **2000**, *4*, 385.

[15] Y. F. Nie, Y. Zhu, C.-H. Lee, L. F. Kourkoutis, J. A. Mundy, J. Junquera, P. Ghosez, D. J. Baek, S. Sung, X. X. Xi, K. M. Shen, D. A. Muller, D. G. Schlom, *Nature Communications* **2014**, *5*, ncomms5530.

[16] J. H. Lee, G. Luo, I. C. Tung, S. H. Chang, Z. Luo, M. Malshe, M. Gadre, A. Bhattacharya, S. M. Nakhmanson, J. A. Eastman, H. Hong, J. Jellinek, D. Morgan, D. D. Fong, J. W. Freeland, *Nature Materials* **2014**, *13*, 879.

[17] D. M. Pozar, *Microwave Engineering*, Wiley, Hoboken, NJ, **2011**.

[18] R. B. Marks, *IEEE Transactions on Microwave Theory and Techniques* **1991**, *39*, 1205.

[19] J. Li, B. Nagaraj, H. Liang, W. Cao, C. H. Lee, R. Ramesh, *Appl. Phys. Lett.* **2004**, *84*, 1174.

[20] J. Li, H. Liang, B. Nagaraj, W. Cao, C. H. Lee, R. Ramesh, *J. Lightwave Technol., JLT* **2003**, *21*, 3282.

[21] J. J. Bussgang, L. Ehrman, J. W. Graham, *Proceedings of the IEEE* **1974**, *62*, 1088.

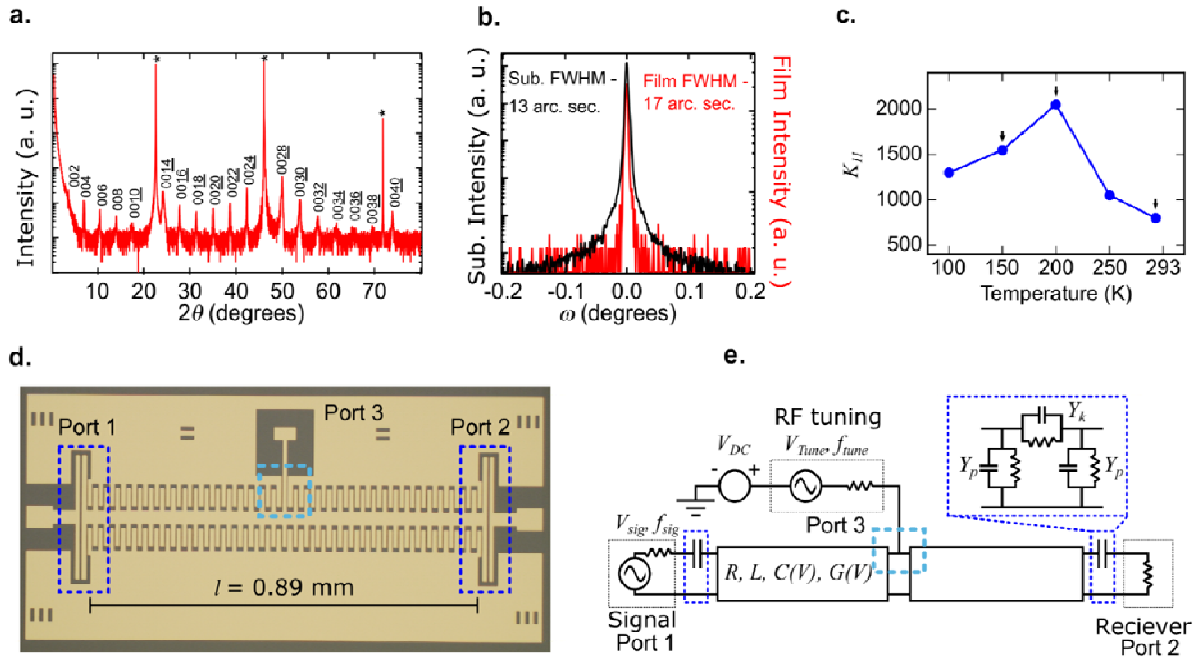

Figure 1. A tunable resonator fabricated on 50 nm thick n = 6 Ruddlesden-Popper $(SrTiO_3)_6SrO$ thin film on (110) $DyScO_3$ with an analytical compact circuit model. a) θ- 2θ XRD characterization of the film. b) Rocking curve data showing high structural quality obtained by MBE deposition. c) Permittivity, K_{11}, as a function of temperature estimated from S-parameter measurements of capacitors and finite element simulation. We see a broad phase transition from ferroelectric to paraelectric states with increasing temperature. Resonator S-parameter and tuning speed measurements were taken at 150 K, 200 K, and 293 K. d) Photograph of a lithographically fabricated resonator, showing the three device

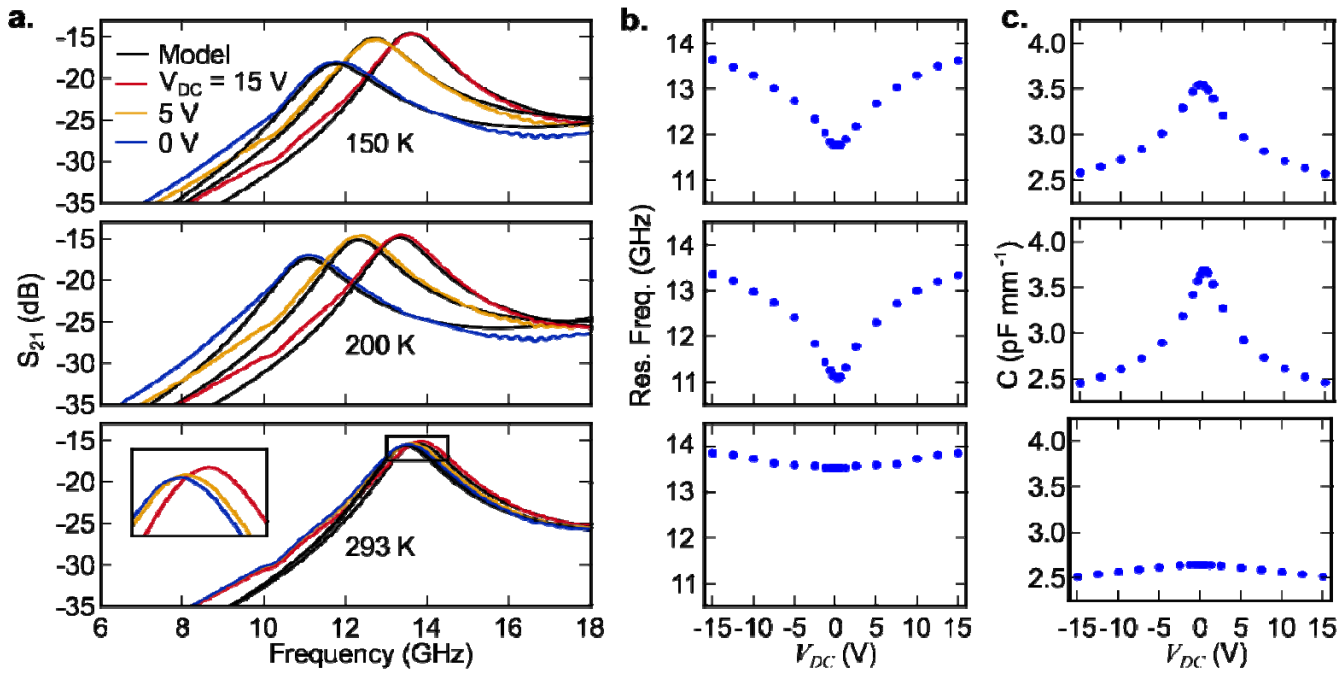

Figure 2. Resonator transmission characterization with DC voltage tuning. a) Transmission coefficient, S_{21}, as a function of temperature and bias voltage. A fit to the circuit model is shown as a black line. b). Resonance frequency as a function of bias voltage for the three temperatures measured. c) Distributed capacitance extracted from a fit to the circuit model shown in Figure 1.e.

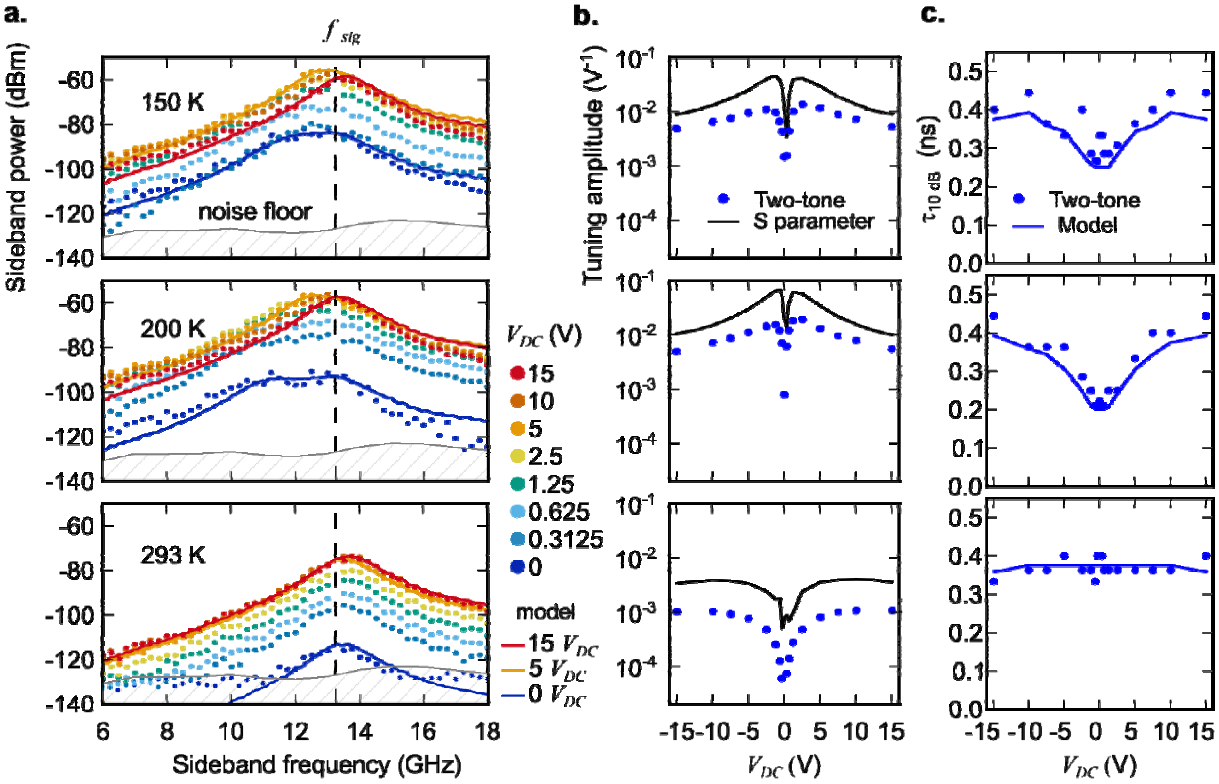

Figure 3. Resonator tuning speed characterization by two-tone frequency-domain measurements. a) Amplitude of sidebands as a function of tuning frequency, bias voltage, and temperature. The dynamic tuning model is shown for V_{DC} = 0 V, 5V, and 15 V as solid lines. The noise floor is the 95th percentile of measurements with no input signal. b) Comparison of the microwave-frequency tuning amplitude, C'/C calculated from the two-tone measurements

with an analogous quantity calculated from S-parameter measurements (Figure 2c). c) The 10-dB tuning time as a function of DC bias voltage, calculated from the two-tone measurements, the S-parameter measurements, and the tuning model. Tuning time is omitted for V_{DC} = 0 V at 293 K, because the peak is not 10 dB above the noise floor.

$(SrTiO_3)_n$SrO Ruddlesden-Popper (RP) superlattices have exceptionally low loss in the 10's of GHz compared with other tunable dielectric materials. This paper reports the first realization of resonators, a ubiquitous building block of microwave components, fabricated on RP films, and an analysis of their static and dynamic tuning behavior. Their tuning speed is limited by circuit properties, rather than materials properties.

Tunable dielectrics

A. M. Hagerstrom*, X. Lu, N. M. Dawley, H. Nair, J. Mateu, R. Horansky, C. A. E. Little, J. C. Booth, C. J. Long, D. G. Schlom, N. D. Orloff

Sub-nanosecond Tuning of Microwave Resonators Fabricated on Ruddlesden-Popper Dielectric Thin Films

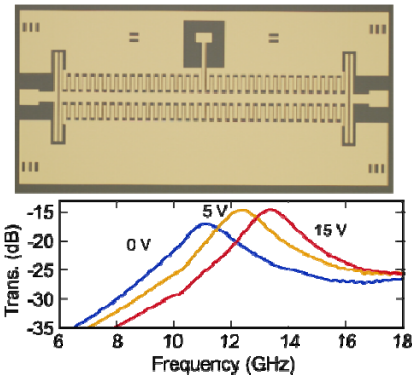

Supporting Information

Sub-nanosecond Tuning of Microwave Resonators Fabricated on Ruddlesden-Popper Dielectric Thin Films

Aaron M. Hagerstrom, Xifeng. Lu, Natalie. M. Dawley, Hari Nair, Jordi Mateu, Robert Horansky, Charles. A. E. Little, James. C. Booth, Christian J. Long, Darrell G. Schlom, and Nathan. D. Orloff*

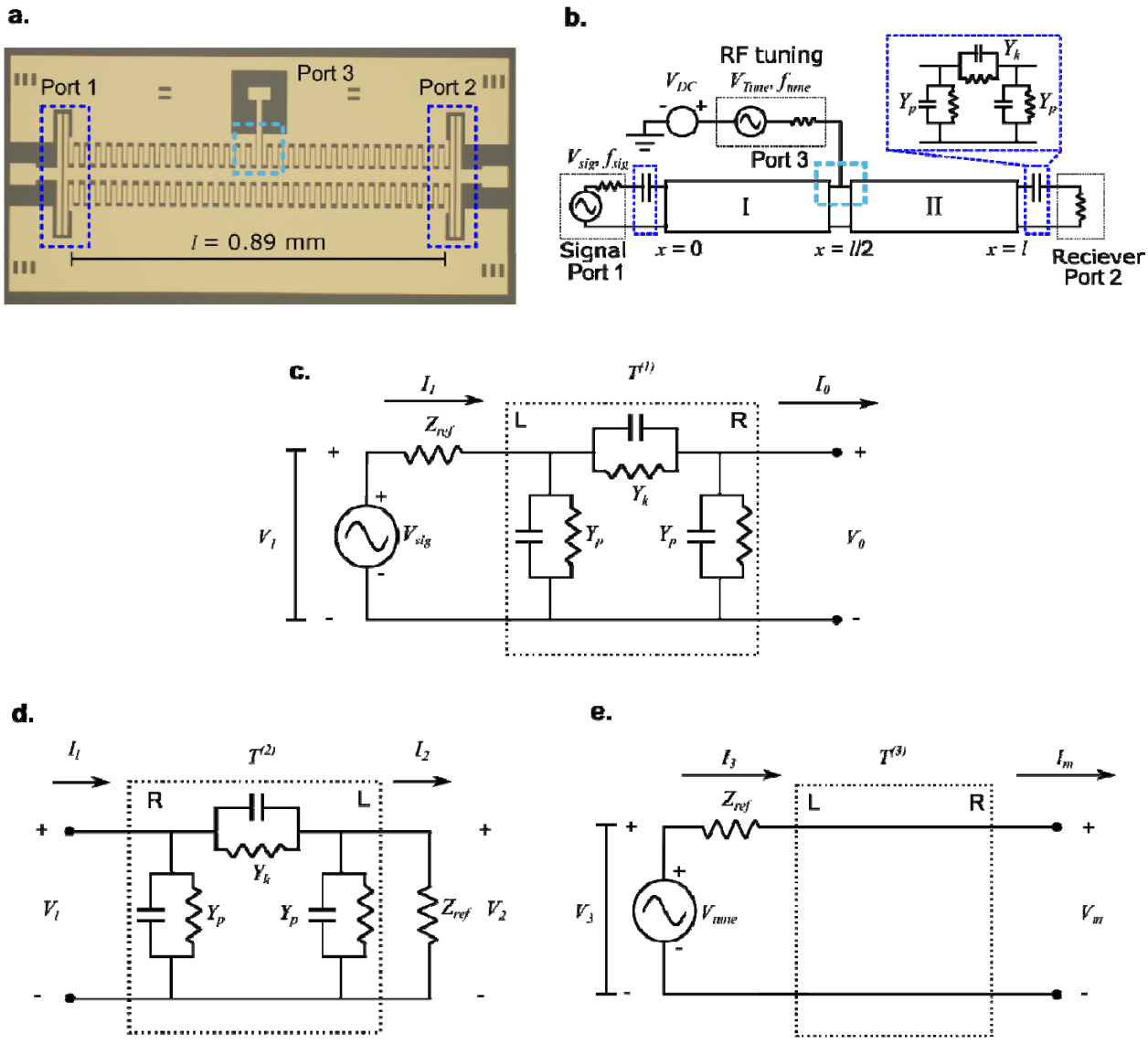

Figure S1. a. Photograph of the device, with coupling capacitors and tuning arm highlighted. b. Circuit model for tunable resonators. Because of the tuning arm, we solve the Telegrapher's equations in two regions, Region I

and Region II, and apply boundary conditions at $x = 0$, $x = l/2$, and $x = l$. The output impedance of the tuning source and the signal source are both $Z_0 = 50\ \Omega$. The input impedance of the spectrum analyzer, also nominally 50 Ω. c. Boundary conditions at port 1. d. Boundary conditions at port 2 e. Boundary conditions at port 3. Circuit parameters are defined in the text.

Overview

Our circuit model provides a physical description of the spatiotemporal structure of all of the signals involved in our measurement, and their coherent nonlinear interactions. Detailed knowledge of this circuit model is not required to interpret the main results, but a detailed description is provided here for completeness. The aim of this section is to completely and explicitly specify the equations we solved in our model, their boundary conditions, and how they were used to generate the theory curves in **Figure 2** and **Figure 3** of the main text.

Figure S1 describes the circuit model. The resonator consists of a transmission line with coupling capacitors at each end and a tuning arm in the middle. The waveguide is parameterized by a distributed resistance R, inductance L, conductance G, and capacitance C. The coupling capacitors are modeled by a network that includes parasitic contributions, with a coupling admittance $Y_k = G_k + j\omega C_k$, and a parasitic admittance to ground $Y_p = G_p + j\omega C_p$. In this model, the tuning of the RP film is reflected by allowing the capacitances (C, C_k, and C_p) and conductances (G, G_k, and G_p) to vary with applied voltage and temperature, while the distributed inductance (L) and resistance (R) are constant with V_{DC}. In order to avoid overfitting, we assumed an idealized frequency dependence of the circuit parameters: L, C, C_k, and C_p were constant with frequency, G, G_k, and G_p were proportional to ω, and R was proportional to $\sqrt{\omega}$. The frequency dependence of these parameters was chosen for qualitative agreement with their expected behavior, because there were not enough devices on the chip to constrain more detailed models.

Nonlinear wave equations

Our goal is to model the spatially distributed currents and voltages in our tunable resonator. It is easier to work in the frequency domain since sinusoidal excitation of our device is both experimentally easy to achieve and amenable to analytical treatment. The voltage and current in the waveguide, as a function of position and time are then:

$$V(x,t) = \sum_m V(\omega_m; x)\exp(j\omega_m t)\,, \#(1)$$

$$I(x,t) = \sum_m I(\omega_m;\ x)\exp(j\omega_m t)\,, \#(2)$$

Because the signals are real, $V(-\omega; x) = V^*(\omega; x)$ and $I(-\omega; x) = I^*(\omega; x)$. In our case, m indexes ω_{sig}, ω_{tune},$-\omega_{sig}$,$-\omega_{tune}$, $\omega_{sig} + \omega_{tune}$, $\omega_{sig} - \omega_{tune}$, $-\omega_{sig} - \omega_{tune}$, $-\omega_{sig} + \omega_{tune}$, but the following discussion can be easily generalized to more tones. To a good approximation, these are the only signals observed experimentally. The first sideband ($\omega_{sig} \pm \omega_{tune}$) has an amplitude of less than -50 dB, compared to 0 dBm for the tuning wave and 8 dBm for the signal wave. The second sideband ($\omega_{sig} \pm 2\omega_{tune}$) has an amplitude of less than -90 dBm. In our analysis, we ignore the second sideband and any higher-order sidebands.

At microwave frequencies, single-mode propagation in a waveguide is traditionally modelled with the telegrapher's equations, which are usually formulated for a wave with a single frequency ω:

$$\frac{dV(\omega; x)}{dx} = -(R + j\omega L)I(\omega; x), \#(3)$$

$$\frac{dI(\omega; x)}{dx} = -(G + j\omega C)V(\omega; x). \#(4)$$

Here, $I(x)$ and $V(x)$ are the current and voltage as a function of position x and time t.

For modes where the electric and magnetic fields are perpendicular to the propagation direction, C and G depend on the dielectric properties of the materials comprising the

waveguide, but R and L do not.[1] We have a tunable dielectric film, so we expect C and G to depend on the applied electric field, and therefore on the voltage. If the voltage varies in space and time, so will the capacitance and conductance. We are also applying a DC bias, which is much larger than our microwave signals. To lowest order, we can make a linear expansion about a DC operating point:

$$C(x,t) = C(V_{DC}) + C' \sum_m V(\omega_m; x) \exp(j\omega_m t)\,, \#(5)$$

$$G(x,t) = G(V_{DC}) + G' \sum_m V(\omega_m; x) \exp(j\omega_m t)\,. \#(6)$$

In general, C' and G' may depend on frequency. In this paper, we assume the quantities to take constant values. When we say that the tuning speed we see is due to circuit properties rather than materials properties, we are referring to the frequency-independence of C' and G'. Equation (5) and Equation (6) state that the capacitance changes instantly in response to an applied voltage. We include both C' and G' for generality, but the current experiment is unable to distinguish between these two, because we measured the nonlinear response using a spectrum analyzer which did not measure the phase of the signal.

The voltage-dependent capacitance and conductance require a modification of the telegrapher's equations. Substituting Equations (5) and Equation (6) into Equation (4), the telegrapher's equations with a voltage-dependent capacitance and conductance are then:

$$\frac{dV(\omega; x)}{dx} = -(R + j\omega L) I(\omega; x), \#(7)$$

$$\frac{dI(\omega; x)}{dx} = -(G + j\omega C) V(\omega; x) - \sum_{\substack{n,m \\ \omega_n + \omega_m = \omega}} (G' + j\omega_n C') V_n(\omega_n; x) V_m(\omega_m; x)\,. \#(8)$$

The equations for the waves at each frequency can be written separately. However, the tuning leads to a nonlinear term. In systems with a 2nd order nonlinearity, pairs of waves with frequencies ω_n and ω_m can mix to generate a wave with a frequency $\omega = \omega_n + \omega_m$. Equation (7) and Equation (8) can be combined into a single 2nd order equation:

$$\frac{d^2}{dx^2}V(\omega;x) = \gamma(\omega)^2\left[V(\omega;x) + \sum_{\substack{n,m \\ \omega_n+\omega_m=\omega}} \frac{G' + j\omega_n C'}{G + j\omega C} V(\omega_m;x)\,V(\omega_n;x)\right]. \#(9)$$

Here $\gamma(\omega) = \sqrt{(R + j\omega L)(G + j\omega C)}$ is the propagation constant.

From Equation (9), the nonlinear mixing products are proportional to:

$$A = \frac{G' + j\omega C'}{G + j\omega C} \approx \frac{C'}{C} \#(10)$$

In the limit that $\omega C \gg G$, i.e. $\tan\delta \ll 1$, $A = C'/C$. In the main text, we refer to the quantity as the "tuning amplitude" (**Figure 3**b). From the point of view of device design, fractional tuning per volt is an intuitive and useful metric. In practice, to compute the tuning amplitude, we set $A = 1$ in Equation (9), compute the nonlinear mixing products, and then compare the computed mixing products to the measured mixing products over the entire bandwidth of the measurement to determine the value of A.

We now develop a perturbative solution to Equation (9). We assume that to lowest order, the sidebands do not affect either the tuning wave or the signal wave. This assumption is experimentally justified because the signal and tuning waves are much larger in amplitude than the sidebands. We solve for $V(\omega_{sig};x)$ and $V(\omega_{tune};x)$ assuming that $V(\omega_{sig}\pm\omega_{tune};x) = 0$. The voltage profiles at all of the relevant frequencies are then given by

$$\frac{d^2}{dx^2}V(\omega_{sig}\pm\omega_{tune};x) = \gamma(\omega_{sig}\pm\omega_{tune})^2 V(\omega_{sig}\pm\omega_{tune};x) + N_{\pm}(x), \#(11)$$

$$\frac{d^2}{dx^2}V(\omega_{sig};x) = \gamma(\omega_{sig})^2 V(\omega_{sig};x), \#(12)$$

$$\frac{d^2}{dx^2}V(\omega_{tune};x) = \gamma(\omega_{tune})^2 V(\omega_{tune};x), \#(13)$$

with the nonlinear term $N_{\pm}(x)$ given by

$$N_{\pm}(x) = \gamma(\omega_{sig}\pm\omega_{tune})^2 \frac{G' + j(\omega_{sig}\pm\omega_{tune})C'}{G + j(\omega_{sig}\pm\omega_{tune})C} V(\pm\omega_{tune};x)V(\omega_{sig};x). \#(14)$$

For now, we focus on the two linear equations, Equation (12) and Equation (13). Once the signal and tuning waves, $V(\omega_{sig}; x)$ and $V(\omega_{tune}; x)$ are known, then $N_{\pm}(x)$ is a known function. At that point, Equation (11) can be solved by a Green's function. For more information on Green's functions, see Reference[2] for a general discussion, and Reference[3] for an application to photoconductive devices which is formally very similar to our current discussion. The tuning arm partitions the waveguide into two regions, labeled I (left half) and II (right half). We can write a general solution to Equation (12) and Equation (13) in regions I and II in terms of unknown constants:

$$V(\omega; x) = \Theta(l/2 - x)V^{I}(\omega; x) + \Theta(x - l/2)V^{II}(\omega; x), \#(15)$$

$$I(\omega; x) = \Theta(l/2 - x)I^{I}(\omega; x) + \Theta(x - l/2)I^{II}(\omega; x), \#(16)$$

$$V^{I}(\omega; x) = V_{+}^{I}\exp(-\gamma x) + V_{-}^{I}\exp(\gamma x), \#\#(17)$$

$$I^{I}(\omega; x) = \frac{V_{+}^{I}}{Z}\exp(-\gamma x) - \frac{V_{-}^{I}}{Z}\exp(\gamma x), \#\#(18)$$

$$V^{II}(\omega; x) = V_{+}^{II}\exp(-\gamma x) + V_{-}^{II}\exp(\gamma x), \#(19)$$

$$I^{II}(\omega; x) = \frac{V_{+}^{II}}{Z}\exp(-\gamma x) - \frac{V_{-}^{II}}{Z}\exp(\gamma x). \#\#(20)$$

Here, $\Theta(x)$ is the unit step function, and $Z = \sqrt{(R + j\omega L)/(G + j\omega C)}$ is the characteristic impedance. The coefficients V_{+}^{I}, V_{-}^{I}, V_{+}^{II}, and V_{-}^{II} are determined by the boundary conditions.

Boundary conditions

In this section we discuss the boundary conditions on port 1 in detail. The discussion for the other ports is very analogous. At the end of the section, we provide a system of equations that solves for the unknown coefficients, taking into account all of the boundary conditions. The boundary conditions can be expressed in terms of transfer (T) parameters. (**Figure S1**c, **S1**d, and **S1**e). These parameters relate the incoming and outgoing power on one port of a device to the incoming and outgoing power on the other port. The T matrix approach has two advantages. First, there are closed-form models available for many circuits, including

our non-ideal coupling capacitors[4]. Second, it's possible to characterize the cables and connectors leading up to a device in terms of T parameters, using linear network analysis. Reference[1] does not give the circuit models in terms of cascade parameters, but it is easy to convert from scattering parameters to T parameters:

$$T_{11} = -\frac{\det(S)}{S_{21}}, \#(21)$$

$$T_{12} = \frac{S_{11}}{S_{21}}, \#(22)$$

$$T_{21} = \frac{-S_{22}}{S_{21}}, \#(23)$$

$$T_{22} = \frac{1}{S_{21}}. \#(24)$$

We will need boundary conditions at $x = l/2$, as well as $x = 0$ and $x = l$. T matrices are formulated in terms of the a and b waves, which are in turn related to voltage and current. For port 1, the a and b waves on both sides of the coupling capacitor are defined as

$$a_1 = \frac{(V_1 + Z_{ref} I_1)}{2\sqrt{Z_{ref}}}, \#(25)$$

$$b_1 = \frac{(V_1 - Z_{ref} I_1)}{2\sqrt{Z_{ref}}}, \#(26)$$

$$a_0 = \frac{(V_0 - Z_{ref} I_0)}{2\sqrt{Z_{ref}}}, \#(27)$$

$$b_0 = \frac{(V_0 + Z_{ref} I_0)}{2\sqrt{Z_{ref}}}. \#(28)$$

Note that the sign of the current is different for a_0 and b_0 compared to a_1 and b_1. This is because the current is conventionally defined as going *into* a device. As shown in Figure **S1**c, I_1 is the current entering the coupling capacitor, but I_0 is the current leaving the capacitor. This unconventional notation is helpful because within the waveguide, current $I(\omega; x)$ is

defined to be positive for current flowing to the right. The T parameters of the coupling capacitor relate a_1, b_1, a_0, and b_0:

$$\begin{pmatrix} b_1 \\ a_1 \end{pmatrix} = \begin{pmatrix} T_{11}^{(1)} & T_{12}^{(1)} \\ T_{21}^{(1)} & T_{22}^{(1)} \end{pmatrix} \begin{pmatrix} a_0 \\ b_0 \end{pmatrix}. \#(29)$$

We will be providing some equations in terms of specific elements of the T matrix, so it is important to be explicit with some of our notation. In **Figure S1**, all of the T matricies are labeled with an "L" and an "R". Quantities on the left-hand side of Equation (29) are labelled with an L and quantities on the right are labeled with an R.

From **Figure S1**c, Ohm's law provides a relationship between V_1 and I_1, which can be used to determine a wave at port 1. This relationship is frequency-dependent: the source will emit power at ω_{sig}, but not ω_{tune}. For the wave at ω_{sig}, from Ohm's law we have $V_1 = V_{sig} - Z_{ref} I_1$, whereas at ω_{tune} we have $V_1 = -Z_{ref} I_1$. We will represent these two situations with a compact notation: $V_1 = V_{sig}[\omega = \omega_{sig}] - Z_{ref} I_1$. $[\omega = \omega_{sig}] = 1$ when discussing the signal wave and $[\omega = \omega_{sig}] = 0$ when discussing the tuning wave. Comparing to Equation (25), this can also be expressed $a_1 = V_{sig}[\omega = \omega_{sig}]/2\sqrt{Z_{ref}}$. The quantity $|a_1|^2$ has units of power and is traditionally interpreted as the power leaving the source. We will treat $|a_1|^2$ as a known quantity, determined by the nominal source power. The boundary condition on port 1 can then be expressed as

$$a_1 = T_{21}^{(1)} a_0 + T_{22}^{(1)} b_0. \#(30)$$

Equation (30) can in turn be expressed in terms of the currents and voltages at the end of the waveguide using Equations (25) and Equation (26):

$$V_{sig}[\omega = \omega_{sig}] = T_{21}^{(1)}(V_0 - Z_0 I_0) + T_{22}^{(1)}(V_0 + Z_0 I_0). \#(31)$$

Equation (30) can be expressed in terms of the coefficients V_+^I, V_-^I

$$V_{sig}[\omega = \omega_{sig}] = (u_1 - z_1)V_+^I + (u_1 + z_1)V_-^I. \#(32)$$

Here, we have introduced the constants:

$$z_i = \frac{Z_{ref}}{Z}\left(T_{22}^{(i)} - T_{21}^{(i)}\right), \#(33)$$

$$u_i = T_{22}^{(i)} + T_{21}^{(i)}. \#(34)$$

The index i indicates that analogous quantities are defined for each of the three ports. There are analogous equations to Equation 14 for the boundary conditions at the other two ports. There is also a fourth boundary condition: the voltage is continuous at the tuning arm. We can collect all of these conditions and express them in matrix notation, $\boldsymbol{AV} = \boldsymbol{B}$:

$$\boldsymbol{A} = \begin{pmatrix} (u_1 + z_1) & (u_1 - z_1) & 0 & 0 \\ 0 & 0 & (u_2 - z_2)e^{\gamma l} & (u_2 + z_2)e^{-\gamma l} \\ (u_3 - 2z_3)e^{\frac{\gamma l}{2}} & (u_3 + 2z_3)e^{\frac{-\gamma l}{2}} & (u_3 + 2z_3)e^{\frac{\gamma l}{2}} & (u_3 - 2z_3)e^{\frac{-\gamma l}{2}} \\ e^{\frac{\gamma l}{2}} & e^{\frac{-\gamma l}{2}} & -e^{\frac{\gamma l}{2}} & -e^{\frac{-\gamma l}{2}} \end{pmatrix}, \#(35)$$

$$\boldsymbol{V} = \begin{pmatrix} V_+^I \\ V_-^I \\ V_+^{II} \\ V_-^{II} \end{pmatrix}, \#(36)$$

$$\boldsymbol{B} = \begin{pmatrix} V_{sig}[\omega = \omega_{sig}] \\ 0 \\ 2V_{tune}[\omega = \omega_{tune}] \\ 0 \end{pmatrix}. \#(37)$$

Scattering parameters

We now have given enough information to describe how to compute the scattering parameters as seen in **Figure 2**.

1. Write down the voltage and current as a function of position for the signal wave, using Equation (15) - Equation(20).
2. Using Equation (35) – Equation (37), solve for the unknown coefficients.
3. Solve for the a and b waves at ports 1 and 2 using Equation (25) – (28), and the analogous equations in terms of the voltages and currents at port 2.
4. The reflection coefficient, S_{11} is given by b_1/a_1

5. The transmission coefficient, S_{21} is given by b_2/a_1.

Sideband solution

The spatial voltage profiles of the sideband waves, $V(\omega_{sig} \pm \omega_{tune}; x)$, are determined by Equation (14), with the boundary conditions given by Equation (15) – Equation(20). Following a standard Green's function approach, we seek a solution to the equation

$$\frac{d^2}{dx^2}\, g(x,y) = \gamma^2 g(x,y) + E\delta(x-y). \#(38)$$

Here $\delta(x-y)$ is a Dirac δ function that models a point-like source at a position y in the waveguide. The constant E has units of Vm^{-1} and has been added to Equation (38) so that the units of the following equations will be more transparent. E has no physical meaning and its value has no effect on the predictions of this model. Once the Green's function $g(x,y)$ is known, it can be used to calculate the solution of Equation (14):

$$V(\omega_{sig} \pm \omega_{tune}, x) = (1/E)\int_0^l dy\; g(x,y) N_{\pm}(y), \#(39)$$

$$I(\omega_{sig} \pm \omega_{tune}, x) = (1/E)\int_0^l dy\; f(x,y) N_{\pm}(y). \#(40)$$

Here, $f = (R + i\omega L)^{-1}\, dg/dx$ is the current associated with the Green's function. One can verify that Equation (39) and Equation (4) satisfy Equation (14) by direct substitution. The Green's function $g(x,y)$ will satisfy the same boundary conditions as the signal and tuning waves, with two additional boundary conditions at the location of the δ function:

$$g(y+\varepsilon, y) - g(y-\varepsilon, y) = 0, \#(41)$$

$$\frac{d}{dx} g(y+\varepsilon, y) - \frac{d}{dx} g(y-\varepsilon, y) = E. \#(42)$$

These equations state that there is a discontinuous jump in the current at the point of the current source and that the voltage is continuous. We can write a general piecewise solution of Equation (38) in terms of unknown coefficients:

$$g(x,y) = \Theta(l/2-y)g^{I}(x,y) + \Theta(y-l/2)g^{II}(x,y), \#(43)$$

$$g^{I}(x,y) = \Theta(l/2-x)\Theta(y-x)\left[g_{+}^{I,L}(y)\exp(-\gamma x) + g_{-}^{I,L}(y)\exp(\gamma x)\right] +$$
$$\Theta(l/2-x)\Theta(x-y)\left[g_{+}^{I,R}(y)\exp(-\gamma x) + g_{-}^{I,R}(y)\exp(\gamma x)\right] +$$
$$\Theta(x-l/2)\left[g_{+}^{I,H}(y)\exp(-\gamma x) + g_{-}^{I,H}(y)\exp(\gamma x)\right], \#(44)$$

$$g^{II}(x,y) = \Theta(l/2-x)\left[g_{+}^{II,H}(y)\exp(-\gamma x) + g_{-}^{II,H}(y)\exp(\gamma x)\right] +$$
$$\Theta(x-l/2)\Theta(x-y)\left[g_{+}^{I,L}(y)\exp(-\gamma x) + g_{-}^{I,L}(y)\exp(\gamma x)\right] +$$
$$\Theta(x-l/2)\Theta(y-x)\left[g_{+}^{I,R}(y)\exp(-\gamma x) + g_{-}^{I,R}(y)\exp(\gamma x)\right]. \#(45)$$

The unknown coefficients in Equations (43) – (45) are the solution to the linear Equations $\boldsymbol{A}^{gI}\boldsymbol{g}^{I} = \boldsymbol{B}^{g}$ and $\boldsymbol{A}^{gII}\boldsymbol{g}^{II} = \boldsymbol{B}^{g}$.

$$\boldsymbol{A}^{gI} = \begin{pmatrix} -e^{\gamma y} & -e^{-\gamma y} & e^{\gamma y} & e^{-\gamma y} & 0 & 0 \\ -e^{\gamma y} & e^{-\gamma y} & e^{\gamma y} & -e^{-\gamma y} & 0 & 0 \\ (u_1+z_1) & (u_1-z_1) & 0 & 0 & 0 & 0 \\ 0 & 0 & 0 & 0 & (u_2-z_2)e^{\gamma l} & (u_2+z_2)e^{-\gamma l} \\ 0 & 0 & (u_3-2z_3)e^{\frac{\gamma l}{2}} & (u_3+2z_3)e^{\frac{-\gamma l}{2}} & (u_3+2z_3)e^{\frac{\gamma l}{2}} & (u_3-2z_3)e^{\frac{-\gamma l}{2}} \\ 0 & 0 & e^{\frac{\gamma l}{2}} & e^{\frac{-\gamma l}{2}} & -e^{\frac{\gamma l}{2}} & -e^{\frac{-\gamma l}{2}} \end{pmatrix}, \#(46)$$

$$\boldsymbol{A}^{gII} = \begin{pmatrix} 0 & 0 & -e^{\gamma y} & -e^{-\gamma y} & e^{\gamma y} & e^{-\gamma y} \\ 0 & 0 & -e^{\gamma y} & e^{-\gamma y} & e^{\gamma y} & -e^{-\gamma y} \\ (u_1+z_1) & (u_1-z_1) & 0 & 0 & 0 & 0 \\ 0 & 0 & 0 & 0 & (u_2-z_2)e^{\gamma l} & (u_2+z_2)e^{-\gamma l} \\ (u_3-2z_3)e^{\frac{\gamma l}{2}} & (u_3+2z_3)e^{\frac{-\gamma l}{2}} & (u_3+2z_3)e^{\frac{\gamma l}{2}} & (u_3-2z_3)e^{\frac{-\gamma l}{2}} & 0 & 0 \\ e^{\frac{\gamma l}{2}} & e^{\frac{-\gamma l}{2}} & -e^{\frac{\gamma l}{2}} & -e^{\frac{-\gamma l}{2}} & 0 & 0 \end{pmatrix}, \#(47)$$

$$\boldsymbol{g}^{I} = \begin{pmatrix} g_{+}^{I,L}(y) \\ g_{-}^{I,L}(y) \\ g_{+}^{I,R}(y) \\ g_{-}^{I,R}(y) \\ g_{+}^{I,H}(y) \\ g_{-}^{I,H}(y) \end{pmatrix}, \boldsymbol{g}^{II} = \begin{pmatrix} g_{+}^{II,H}(y) \\ g_{-}^{II,H}(y) \\ g_{+}^{II,L}(y) \\ g_{-}^{II,L}(y) \\ g_{+}^{II,R}(y) \\ g_{-}^{II,R}(y) \end{pmatrix}, \boldsymbol{B}^{g} = \begin{pmatrix} 0 \\ \frac{E}{\gamma} \\ 0 \\ 0 \\ 0 \\ 0 \end{pmatrix}. \#(48)$$

Sideband power

We now have given enough information to describe how to compute the sideband power seen in **Figure 2**.

1. Write down the voltage and current as a function of position for the signal wave, using Equation (15) - Equation (20).
2. Using Equation (35) - Equation (37), solve for the unknown coefficients.
3. From Equation (14), compute the nonlinear source term.
4. From Equation (46) – (48), compute the Greens function. Note that this procedure of calculating the Green's function must be repeated for each value of y.
5. From Equation (39) and Equation (40), compute the current and voltage.
6. From Equation (25) – Equation (28), compute the a and b waves at port 2.
7. The sideband power is $|b_2|^2$.

Discussion of nonlinear measurement uncertainty

Assigning uncertainty to nonlinear microwave-frequency measurements is an active area of research.[5] Random noise is rarely the leading contribution to uncertainty in microwave measurements. Instead, measurement errors are usually correlated between frequency points and strongly frequency dependent. These errors can arise from the non-ideal electrical characteristics of the measurement apparatus, such as uncharacterized standing waves in the cables leading up to the device under test, and imperfect definitions of calibration standards. For several reasons, the approach of reference[5] is not appropriate to our experiment. The most compelling reason is that our device had three ports and developing an appropriate on-wafer calibration procedure and calibration standards for a three-port measurement is a non-trivial endeavor. A second reason that we could not use the existing approaches is that we used a spectrum analyzer to detect the amplitude of our nonlinear signal. This instrument does not measure phase of the signal, nor does it measure the a and b

waves independently. These data are necessary for constructing a calibration and uncertainty analysis. That said, we can estimate uncertainty in qualitative way. Using the residuals of our model fit in **Figure 3**b near resonance, we estimate that the uncertainty in the tuning amplitude is about 10%. From the scatter in the points in **Figure 3**c, we estimate the uncertainty of the tuning time measurements to be about 0.05 ns. Future work will focus on more accurate calibration and uncertainty quantification.

References

[1] R. B. Marks, D. F. Williams, *J. Res. Natl. Inst. Stand. Technol.* **1992**, *97*, 533.

[2] I. Stakgold, M. J. Holst, *Green's Functions and Boundary Value Problems*, John Wiley & Sons, **2011**.

[3] M. Neshat, D. Saeedkia, S. Safavi-Naeini, *Int. J. Infrared Millim. Waves* **2008**, *29*, 809.

[4] D. M. Pozar, *Microwave Engineering*, Wiley, Hoboken, NJ, **2011**.

[5] G. Avolio, A. Raffo, J. Jargon, P. D. Hale, D. M. M. P. Schreurs, D. F. Williams, *IEEE Trans. Microw. Theory Tech.* **2015**, *63*, 2353.

[6] D. E. Root, J. Verspecht, J. Horn, M. Marcu, *X-Parameters: Characterization, Modeling, and Design of Nonlinear RF and Microwave Components*, Cambridge University Press, **2013**.